
Prototype of a Free Space Optical Link for Quantum Communications

Lucía Guerrero Muñoz

Supervised by: José María Gómez Cama, José Bosch Estrada

Department of Quantum Physics and Astrophysics

University of Barcelona

6 July 2025



**Master in Quantum
Science and Technology**
Barcelona

Abstract

This Master's thesis presents the development of a free-space optical link for quantum communications, followed by the design and characterization of the single-photon source used to power it. A laboratory-scale link was established using Ritchey–Chrétien telescopes. To overcome the central obstruction of the telescopes, two different methods were tested: the use of axicon lenses to shape the beam into a toroidal beam with a Bessel-Gaussian profile and the lateral displacement of the input beam. The latter enabled successful photon transmission, revealing a bunching measurement in the second order cross-correlation function at the expected arrival time difference between the heralding photons and the signal ones measured at the receiver of 44 coincident counts per minute.

To provide the required quantum light source, an entangled-photon source based on spontaneous parametric down-conversion in beta barium borate crystals was developed. Pairs of polarization-entangled photons at 810 nm were produced and verified using a CHSH inequality test, which resulted in a Bell parameter of $S = 2.55 \pm 0.15$, which confirms the presence of quantum entanglement.

Keywords: Single-Photons, SPDC, CHSH, Free-Space Communication, Axicons, Telescopes

Acknowledgements

This study was supported by MCIN with funding from European Union NextGenerationEU (PRTR-C17.I1) and by Generalitat de Catalunya. We acknowledge funding from Grants PID2023-147475NB-I00 and CEX2024-001451-M financed by MCIN/AEI/10.13039/50110-0011033 and Grants 2021SGR01095, and 2021SGR01108 by Generalitat de Catalunya. This project has received funding from the European Union's Digital Europe Programme under grant agreement no. 101084035.

Now, first of all, I am deeply thankful to my supervisors, José María Gómez and José Bosch, for all the exciting discussions in the lab, for their kindness, and for their unwavering support.

I am also grateful to Bruno Julià Díaz for his guidance and assistance over these past months.

I want to express my appreciation and admiration to my colleagues from the QComm-sUB group. Especially to Lidia, Raúl and Adrià; for the shared ideas, unconditional help and good energy. And of course, to my friend and daily companion on the front lines, Berkant.

A special mention goes to Annika and Julie, the best gift this Master has given me. And to Juampi, the best partner in crime I could have asked for.

Finally, I want to dedicate this work to my family: my parents, Ana and Enrique; my siblings, Guille and Claudia; and my grandmother, la Yaya. All my accomplishments will always be yours as well.

Contents

1	Introduction	3
2	Theoretical Background	4
2.1	Free-Space Quantum Channels	4
2.2	Emitter	5
2.2.1	Spontaneous Parametric Down-Conversion	5
2.2.2	The CHSH Inequality	7
2.3	Receiver	8
2.3.1	Second-Order Correlation Function	8
3	Experimental Setup	9
3.1	Channel Access	9
3.2	Emitter	12
3.3	Receiver	14
4	Results and Discussion	15
4.1	Tuning the Pumping Beam	15
4.2	Characterization of the Entangled Photon Source	16
4.3	Coincident Counts Through the Link	18
4.4	Discussion of Key Rates	21
5	Conclusions	21
	Bibliography	23
A	Coincident Counts	27
B	Probabilities and Uncertainties	27
C	Bell Test Experimental Data	28
D	List of Material	29

1 Introduction

The need for secure communication is deeply embedded in human society. As digital infrastructure expands and more sensitive data is transmitted online, ensuring the confidentiality and integrity of information becomes increasingly critical. Traditional cryptographic protocols such as RSA [35], based on the assumed computational intractability of certain mathematical problems, are now facing a growing threat from quantum computing. This has prompted a fundamental re-evaluation of how secure communication can be guaranteed.

Quantum technologies offer a radically different approach. By leveraging the inherent randomness and measurement sensitivity of quantum mechanics, Quantum Key Distribution (QKD) allows two parties to generate a shared secret key with unconditional security, protected by physical laws rather than computational assumptions [32]. Since its first experimental demonstrations in the 1990s [4], QKD has made significant progress, especially in optical fiber networks where long-distance and high-rate key exchange has become commercially feasible [26, 43].

However, fiber-based QKD is fundamentally constrained by exponential photon loss with distance [38] and susceptibility to dispersion and polarization drift. To overcome these limitations, free-space optical communication (FSO) has emerged as a promising alternative, especially for long-distance or satellite-based implementations. Unlike fibers, atmospheric channels primarily introduce attenuation in the lower 10–20 km and offer superior polarization preservation over long distances [5].

The first real-world free-space QKD link was demonstrated in Singapore in 2006 over a 1.5 km urban line-of-sight link between two buildings [19]. Since then, enormous progress has been made: entanglement-based QKD has been demonstrated over 144 km between the Canary Islands [40], and secure quantum links have been successfully extended into space. China’s Micius satellite mission marked a major milestone by distributing entangled photons across 1200 km between two ground stations and enabling satellite-to-ground QKD [22]. In Europe, the EAGLE-1 mission [6] also explore satellite-based QKD using decoy-state protocols, with a launch planned for 2025.

These satellite-based systems often use weak coherent pulses for simplicity and robustness, but this approach has limitations. In particular, it is susceptible to side-channel attacks and requires trust in the devices used [23]. In contrast, entanglement-based QKD and true single-photon sources offer distinct advantages: they can enable device-independent security and allow for fundamental tests of quantum physics over large distances [20].

Despite these promising features, the implementation of entangled-photon sources in free-space links remains a technical challenge. Efficiently coupling quantum light into telescopes, compensating for alignment drifts, and maintaining entanglement fidelity over atmospheric channels all require precise engineering and system-level integration [41].

A project to establish a city-scale quantum communication network in Barcelona is being developed. It is planned to have different nodes at institutions such as the University of Barcelona (UB), ICFO, the Fabra Observatory, I2Cat and Ramón Llull University. Conducted within the QCommsUB research group at UB, this thesis contributes to address part of this challenge by **developing and demonstrating a laboratory-based prototype FSO quantum link powered by an entangled photon source**. This includes:

- Development of a free-space optical link using Ritchey–Chrétien telescopes.
- Design and characterization of an entangled photon source suitable for free-space QKD.

With the aim to have a future UB–Fabra FSO link.

This thesis begins with an overview of the theoretical foundations underpinning FSO channels, single-photon sources and single-photon detection. It then details the design and implementation of our laboratory-scale free-space link, including the implementation and characterization of a heralded single-photon source. Finally, single-photon transmission measurements are discussed together with the entanglement characterization via a Bell test of the entangled-photon source. The work concludes with a summary of the prototype’s performance and a discussion of opportunities for scaling to longer urban links.

2 Theoretical Background

The successful implementation of a QKD link requires (as any communication link) the careful integration of three essential components: the channel, the emitter, and the receiver. Each element must be engineered to preserve the quantum properties of the transmitted photons while minimizing losses and noise.

In this section, the theoretical principles underlying the design and operation of the prototype free-space quantum link are presented. First, the characteristics of the FSO channel and its interaction with the atmosphere are described. The emitter is then analyzed, with particular attention to the choice of the single-photon source used in this work. Finally, the architecture of the receiver is discussed, along with the strategy followed to demonstrate the successful reception of single photons through the link.

2.1 Free-Space Quantum Channels

FSO links are widely regarded as a key technology for enabling global-scale quantum networks. By transmitting quantum signals through the atmosphere without relying on physical infrastructure, FSO systems offer great flexibility and are suitable for both satellite-based and ground-based QKD implementations.

A significant advantage of FSO channels is their ability to preserve the polarization state of photons to a high degree, making them particularly well-suited for polarization-encoded quantum protocols [30]. However, atmospheric absorption must be carefully considered when selecting the operational wavelength of the quantum signal. Specific absorption bands caused by water vapor, aerosols, and other atmospheric constituents can significantly attenuate photon transmission [11].

To maintain stable optical alignment in the presence of dynamic atmospheric conditions, FSO systems typically employ classical beacon lasers at a wavelength distinct from the quantum signal. These beacons enable the implementation of pointing, acquisition, and tracking (PAT) systems, which actively compensate for slow drifts or rapid fluctuations in the optical path introduced by turbulence [22]. Atmospheric turbulence distorts the wavefront of the beam, leading to fluctuations in phase and angle-of-arrival, which degrade coupling efficiency. In some cases, adaptive optics can be integrated to correct for these distortions in real time [1].

Beyond turbulence, free-space optical channels are also fundamentally limited by diffraction, which causes even an ideal, collimated beam to diverge as it propagates. This diffraction-induced beam expansion increases with distance and is more pronounced for beams with smaller waists or longer wavelengths. As a result, the photon flux arriving at the receiver decreases with distance, regardless of atmospheric quality. When combined with atmospheric turbulence, which further causes beam wandering and wavefront distortion, the spatial coherence and focus of the beam degrade significantly. To mitigate these

effects, large receiving optics are used to increase photon collection efficiency [24].

2.2 Emitter

In a quantum communication system, the emitter, commonly referred to as Alice, functions as the encoding module, tasked with preparing quantum states in accordance with the selected protocol [39]. Information is encoded onto a specific quantum degree of freedom of a single photon, such as polarization, phase, or time-bin, depending on the implementation. The quality and stability of this state preparation are crucial for ensuring high-fidelity transmission across the quantum channel.

To establish a quantum communication link, an emitter encodes information in the selected quantum degree of freedom. Photon sources used in quantum communication can be broadly categorized as either deterministic or statistical. Deterministic sources, such as quantum dots [34], nitrogen-vacancy centers in diamond [2], or trapped atoms and ions [13], are engineered to emit a single photon on demand. These systems typically offer high purity and indistinguishability but often require cryogenic temperatures or complex setups, limiting their scalability in some free-space implementations.

In contrast, statistical photon sources, such as those based on spontaneous parametric down-conversion (SPDC) [10] or spontaneous four-wave mixing (SFWM) [3], operate probabilistically and do not emit a fixed number of photons per excitation pulse. The inherent randomness of these sources can be mitigated using techniques like spatial multiplexing [18], which involve operating multiple identical sources in parallel and routing the successfully heralded photons from any of them into a common output mode. This approach increases the overall probability of obtaining a single photon, while maintaining a low excitation power to ensure that the likelihood of generating multiple photon pairs simultaneously remains negligible.

In the following subsection, the physics underlying SPDC is discussed.

2.2.1 Spontaneous Parametric Down-Conversion

SPDC is a nonlinear optical process widely used in quantum optics to generate photon pairs with strong quantum correlations [37]. When a high-energy pump photon propagates through a nonlinear crystal, it can spontaneously decay into two lower-energy photons, commonly referred to as the signal and idler, under the constraints of energy and momentum conservation. The process is facilitated by the second-order nonlinearity of the medium and does not require external stimulation.

SPDC can occur in different phase-matching configurations, classified as Type-0, Type-I, or Type-II, depending on the polarization relationships among the pump, signal, and idler photons [36]. A variety of nonlinear crystals can be used to implement SPDC, chosen based on the desired phase-matching conditions, operational wavelength, and efficiency. When properly engineered, the emission cones of photon pairs from different polarization processes can overlap spatially and temporally, enabling the generation of polarization-entangled states. Traditionally, β -barium borate (BBO) crystals have been widely used for generating polarization-entangled photon pairs via SPDC [9], particularly in early landmark experiments in quantum information. However, more recently, periodically poled crystals, such as periodically poled potassium titanyl phosphate (PPKTP) [15], have become increasingly favored due to their higher brightness and more efficient photon collection.

Entangled photon pairs can be produced by directing a diagonally polarized pump beam into two orthogonally oriented Type-I phase-matched crystals placed in contact.

In this configuration, one crystal down-converts horizontally polarized pump photons into vertically polarized photon pairs, while the other crystal converts vertically polarized pump photons into horizontally polarized pairs. The down-conversion processes are represented as:

$$|H\rangle_{\text{pump}} \xrightarrow{\text{SPDC}^{(1)}} |V\rangle_s \otimes |V\rangle_i, \quad (1)$$

$$|V\rangle_{\text{pump}} \xrightarrow{\text{SPDC}^{(2)}} e^{i\phi} |H\rangle_s \otimes |H\rangle_i, \quad (2)$$

where ϕ represents a relative phase difference introduced due to optical path differences or birefringence in the medium. When the pump beam is prepared in a diagonal polarization state:

$$|\Psi\rangle_{\text{pump}} = \frac{1}{\sqrt{2}} (|H\rangle + e^{i\varphi} |V\rangle), \quad (3)$$

the photon pairs can originate from either crystal. In the spatial and temporal overlap region of their emission cones, the photons become indistinguishable, allowing quantum interference to occur. This results in an entangled state of the form:

$$|\Psi\rangle = \frac{1}{\sqrt{2}} (|VV\rangle + e^{i(\varphi+\phi)} |HH\rangle). \quad (4)$$

By controlling the relative phase $\varphi + \phi$, one can tailor the quantum state to produce specific Bell states. For example, when the total phase is zero or π , the generated state corresponds to:

$$\varphi + \phi = 0 \Rightarrow |\Phi^+\rangle = \frac{1}{\sqrt{2}} (|VV\rangle + |HH\rangle), \quad (5)$$

$$\varphi + \phi = \pi \Rightarrow |\Phi^-\rangle = \frac{1}{\sqrt{2}} (|VV\rangle - |HH\rangle). \quad (6)$$

Additional optical elements such as a half-wave plate placed in the signal or idler arms can be used to generate the full set of four Bell states. These entangled photon pairs are instrumental in various quantum communication protocols, including quantum key distribution, quantum teleportation, and quantum repeaters.

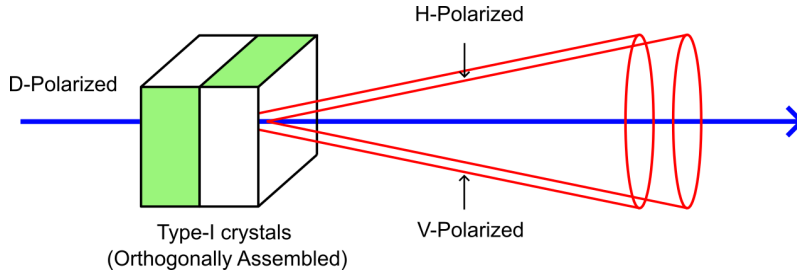


Figure 1: Schematic representation of the SPDC process in a pair of orthogonally oriented Type-I crystals. The emission cones overlap, enabling the generation of polarization-entangled photon pairs.

One effective way to verify entanglement between photon pairs is through the violation of a Bell inequality [27], as discussed in the following subsection.

2.2.2 The CHSH Inequality

The Clauser-Horne-Shimony-Holt (CHSH) inequality [8] is the most well-known and experimentally accessible form of Bell's inequality. It provides a clear criterion for distinguishing quantum correlations from those permitted by classical local hidden variable theories.

According to the CHSH formulation, measurements are performed on two subsystems of a bipartite quantum state, typically by spatially separated observers, conventionally named Alice and Bob. Each observer independently chooses between two possible measurement settings. The outcomes of these measurements are used to calculate a correlation function $E(\alpha, \beta)$, where α and β represent the chosen settings for Alice and Bob, respectively.

In classical theories based on local realism, the CHSH parameter S , defined as a specific linear combination of four correlation functions, is constrained by the inequality:

$$|S| \leq 2 \quad (\text{classical bound})$$

Quantum mechanics, however, predicts that entangled states can exhibit stronger correlations, allowing this bound to be violated. For maximally entangled states, the CHSH parameter can reach:

$$|S| = 2\sqrt{2}$$

A measured value of $|S| > 2$ thus constitutes clear evidence of quantum entanglement and non-local correlations.

To test the CHSH inequality in a typical polarization-based scenario, polarization measurements are performed on entangled photon pairs. Alice and Bob each choose between two linear polarization settings:

- Alice: $\alpha_1 = 0^\circ$ and $\alpha_2 = 45^\circ$
- Bob: $\beta_1 = 22.5^\circ$ and $\beta_2 = -22.5^\circ$

These angles are selected to maximize the expected quantum violation of the inequality. For each angle pair (α, β) , coincidence counts are collected for the four possible outcomes: both photons transmitted (HH), one transmitted and one reflected (HV, VH), and both reflected (VV). The correlation function is then computed as:

$$E(\alpha, \beta) = P_{VV} - P_{VH} - P_{HV} + P_{HH}$$

where P_{ij} denotes the normalized probability of detecting the respective coincidence outcome.

With the four relevant correlation values, the CHSH parameter is calculated as:

$$S = E(\alpha_1, \beta_1) + E(\alpha_1, \beta_2) + E(\alpha_2, \beta_1) - E(\alpha_2, \beta_2)$$

If the resulting value satisfies $|S| > 2$, the state under test cannot be explained by classical local hidden variable models, thus confirming the presence of quantum entanglement. Such tests provide a powerful and operationally meaningful criterion for verifying non-classical correlations in quantum systems.

2.3 Receiver

The receiver, commonly referred to as Bob, serves as the decoding module, responsible for measuring the quantum states transmitted through the optical channel. This is accomplished using detection modules tailored to the encoding basis employed.

To verify the quantum nature of the received light and assess whether single photons are being transmitted through the channel, one commonly used technique at the receiver is antibunching measurement [12]. This approach exploits the fact that true single-photon sources exhibit photon antibunching behavior, meaning that the probability of detecting two photons simultaneously is strongly suppressed. Observing such behavior provides strong evidence that the light field contains predominantly one photon at a time, rather than classical or multi-photon states.

Another widely adopted technique, especially in systems using heralded single-photon sources [7], is based on coincidence measurements between signal photons transmitted through the quantum channel and their corresponding heralding photons. These sources, typically based on spontaneous parametric down-conversion (SPDC), generate photon pairs probabilistically. While they do not emit single photons deterministically, they most often emit either zero or one photon pair per pump pulse, with a much lower probability of emitting two or more pairs. Moreover, in the rare event of multi-pair generation, transmission losses often prevent all photons from reaching the detectors. As a result, under typical operating conditions, the detection of a heralding photon is a strong statistical indicator that its partner photon is present and alone in the signal channel.

One effective way to verify single-photon transmission through such coincidence-based strategies is through second-order correlation measurements, as described in the following subsection.

2.3.1 Second-Order Correlation Function

Theoretically, the second-order correlation function [21] is defined as:

$$g^{(2)}(t, t + \tau) = \frac{\langle I(t)I(t + \tau) \rangle}{\langle I(t) \rangle \langle I(t + \tau) \rangle},$$

where $I(t)$ denotes the photon intensity at time t , and angle brackets indicate a temporal or ensemble average.

In practice, the measurement system registers a coincidence histogram according to:

$$C(\tau) = \sum_t I_1(t) \cdot I_2(t + \tau),$$

with $I_1(t)$ and $I_2(t + \tau)$ representing binary indicators of photon detection events in the two channels.

To extract relevant physical information, the raw counts are integrated over a coincidence window centered around $\tau = 0$:

$$C_{\text{window}} = \sum_{\tau=\tau_{\min}}^{\tau_{\max}} C(\tau),$$

and the corresponding coincidence rate is obtained by normalizing over the total acquisition time:

$$R_{\text{coinc}} = \frac{C_{\text{window}}}{T_{\text{acq}}}.$$

Finally, normalization of the coincidence counts yields the second-order correlation function:

$$g^{(2)}(\tau) = \frac{C(\tau)}{R_1 \cdot R_2 \cdot \Delta t \cdot T_{\text{acq}}},$$

where R_1 and R_2 are the average single-channel count rates, Δt is the time bin width, and T_{acq} is the acquisition duration.

This normalized correlation function enables a clear physical interpretation: $g^{(2)}(0) < 1$ indicates antibunching, a signature of single-photon emission, $g^{(2)}(0) = 1$ is consistent with Poissonian statistics and $g^{(2)}(0) > 1$ reveals photon bunching typically observed in thermal light sources or, in this case case, observed in coincident detection of the heralded and the signal photons.

3 Experimental Setup

The experimental setup comprises three main components: the access to the free-space optical channel, the emitter, and the receiver. An overview of the integrated system is shown in Fig. 2. All materials used in this work are listed in Appendix D.

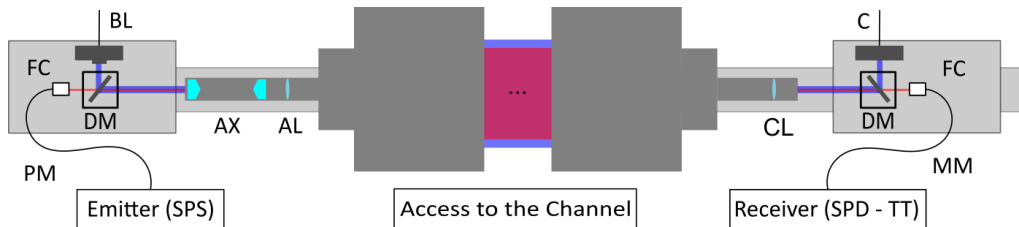


Figure 2: Schematic of the free-space quantum communication link. The emitter module includes a single-photon source (SPS) coupled into a polarization-maintaining (PM) fiber and connected to a fiber coupler (FC). Photons are directed through a dichroic mirror (DM), and the beam is shaped by a pair of axicons (AX) and an achromatic lens (AL). The Access to the Channel includes alignment and monitoring components such as the beacon laser (BL) and the camera (C). In the receiver, the beam is collected with a convex lens (CL), directed through a DM, and coupled via a fiber coupler (FC) into a multimode (MM) fiber for detection by a single-photon detector (SPD) connected to a time tagger (TT). This schematic represents the initial planned configuration, including the use of a beacon laser and PM fiber. Mirrors were later added before the FC in the receiver to improve coupling efficiency.

3.1 Channel Access

To efficiently transmit single photons through free space, the optical system needed to provide collimation and reliable alignment. Although the lab-scale link spans a relatively short distance, the setup was designed with future long-range applications in mind, such as urban or satellite-based quantum communication. For this reason, Ritchey–Chrétien reflective telescopes (TS-Optics 12” Ritchey–Chrétien, Teleskop Service) were chosen for both transmission and reception [22].

A challenge arose from the secondary mirror in the emitter telescope, which becomes a 152 mm diameter central obstruction along the optical axis (see Fig. 3). To address this, it was necessary to reshape or redirect the beam to avoid the blocked region while maintaining transmission quality.

One solution is to generate a Bessel-Gaussian beam using a pair of axicons, following the design in [29]. This beam has a ring-shaped intensity profile that naturally avoids the obstruction and offers lower diffraction, beneficial for long-distance propagation.

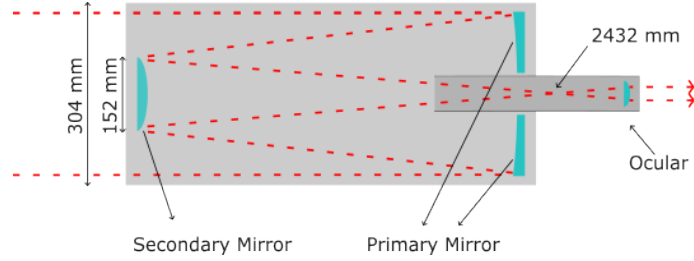


Figure 3: Schematic of the TS-Optics 12" Ritchey-Chrétien (RC) reflective telescope, with a 304 mm aperture and a 2432 mm focal length, used in the experimental free-space optical link.

To make this configuration practical, the input beam size needed to be reduced. Light emitted from the fiber-coupling lens (F810FC-780, Thorlabs) had a diameter of approximately 18 mm:

$$D = 2f \cdot NA = 2 \cdot 36.01 \text{ mm} \cdot 0.25 = 18.01 \text{ mm}. \quad (7)$$

This diameter was too large for the axicon spacing. To reduce it, a beam-reduction telescope was constructed using a pair of plano-convex lenses with focal lengths of 125 mm (LA1986-A-ML, Thorlabs) and 35 mm (LA1027-A-ML, Thorlabs), resulting in a demagnification ratio of 0.28, which scaled the beam diameter down to 5.1 mm. Simulations (Fig. 4) and experimental profiles (Fig. 5) confirmed that this produced a clean, stable Bessel-Gaussian ring of 3.72 mm RMS radius.

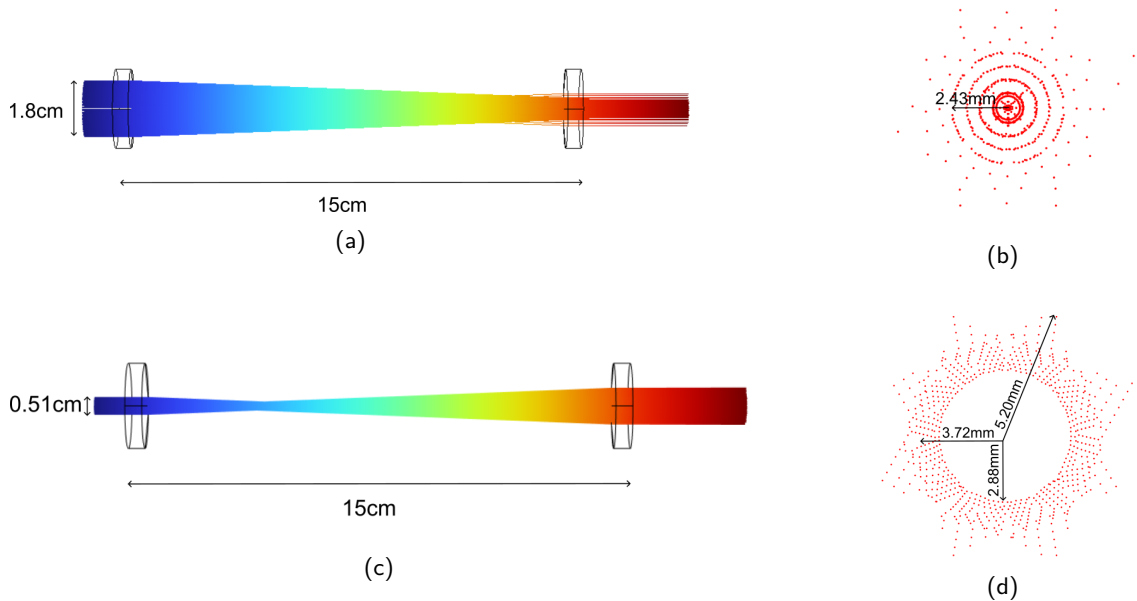


Figure 4: COMSOL simulations. (a) Beam entering the axicons with original diameter. (b) Transverse pattern with unstable interference. (c) Reduced-diameter beam. (d) Stable Bessel-Gaussian ring output.

This corresponds to a projected RMS ring diameter of approximately 25 cm at the telescope output, large enough to clear the 15.2 cm central obstruction yet comfortably within the 30.4 cm aperture. The magnification is given by the ratio of the telescope's focal length, 2432 mm, to the focal length of the achromatic lens used for collimation (9-794, Edmund Optics), 72 mm, yielding a factor of 33.78.

An alternative approach was also tested: launching the beam off-axis with its waist at



Figure 5: Ring profile observed at the second axicon output and at the achromatic lens using a fiber-coupled alignment lamp (VLP50, NetPeppers).

the telescope's focal plane to avoid the obstruction without shaping optics. While simpler, this configuration lacked the advantages of the axicon beam, such as reduced divergence and improved robustness. The larger beam size from the axicons also made alignment easier and more tolerant to small setup variations.

To aid alignment, a 405 nm classical beacon laser was considered. It would have been injected into the optical path via a dichroic mirror and extracted at the receiver for imaging with a tracking camera. This would provide real-time feedback for alignment without affecting the quantum signal. However, given the stable lab environment and negligible turbulence, active tracking was unnecessary, and the beacon laser was ultimately omitted.

All experiments were conducted in a temperature-controlled room at $24^\circ \pm 5^\circ\text{C}$, with minimal ambient light and negligible air currents, ensuring stable transmission conditions and consistent beam quality.

Initial collimation was verified using a 650 nm guiding laser (2" collimator, Howie Glatter), projected onto the covered receiver aperture. The formation of concentric rings (Fig. 6) confirmed proper alignment.



Figure 6: Projection from the emitter telescope onto the covered receiver telescope, showing concentric ring formation with the guiding laser (2" collimator, Howie Glatter).

The telescope focal planes were located by imaging distant outdoor objects with a sensor camera. Once set, the telescopes were mounted on optical tables with custom-machined aluminum supports and laterally aligned. Final adjustments were made using an alignment laser, distinct from the beacon laser, consisting of a laser lamp connected to the fiber feeding the FC. This allowed the light to follow the same optical path as the single photons, enabling fine-tuning to ensure clean coupling into the receiver.

3.2 Emitter

For the purposes of testing the free-space optical channel in this work, the emitter is realized as a heralded single-photon source based on SPDC. This choice enables temporal correlation between the generated photon pairs, which is ideal for coincidence-based measurements and characterizations. Among various single-photon generation methods, SPDC was selected for two main reasons: the typical wavelength of the down-converted photons (810 nm) lies in a spectral window suitable for atmospheric transmission [11], and BBO crystals required for SPDC were readily available in the laboratory.

No active polarization encoding was applied; the goal was to generate entangled photon pairs and send one of them through the channel in a fixed polarization basis. The final layout is shown in Fig. 7.



Figure 7: Experimental set-up of the entangled-photon collection.

When pumped with diagonally polarized 405 nm light from a laser, the source emits photon pairs at 810 nm via spontaneous parametric down-conversion. The pump beam is prepared using a 405 nm bandpass filter (FBH405-10, Thorlabs) and a linear polarizer (LPVISE100-A, Thorlabs) to enforce horizontal polarization, followed by a half-wave plate (WPH05M-405, Thorlabs) to rotate it to diagonal.

The emission from the BBO crystals is collimated with an achromatic lens (49-794, Edmund Optics), while residual pump light is blocked by an 800 nm bandpass filter (FBH800-40, Thorlabs).

A right-angle prism (MRAK25-P01, Thorlabs) then splits the emission into two spatial modes (Fig. 8b). Each output arm is directed using a pair of dielectric mirrors (BB1-E03, Thorlabs) and coupled into a fiber via a fiber collimator (F810FC-780, Thorlabs), all mounted on kinematic stages for precision alignment. The signal photon is launched into a polarization-maintaining single-mode fiber (P3-630PM-FC-2, Thorlabs) for quantum transmission, while the idler is collected into a multimode fiber (M43L05, Thorlabs) serving as the heralding photon.

Accurate fiber coupling required aligning the 405 nm pump beam horizontally relative to the optical table. This was achieved with two mirrors (BB1-E02, Thorlabs) steering the beam through a pair of pinholes (IDA15/M-P5) placed at equal heights and spaced several tens of centimeters apart, establishing a horizontal reference.

Once the path was established, a right-angle mirror (BSH1/M, Thorlabs) redirected the emission toward the coupling optics. For an initial coarse alignment, each of these new paths was back-illuminated with a visible lamp (VLP50, NetPeppers) connected to the fibers, allowing the reverse-propagating light to target the BBO crystals [31].

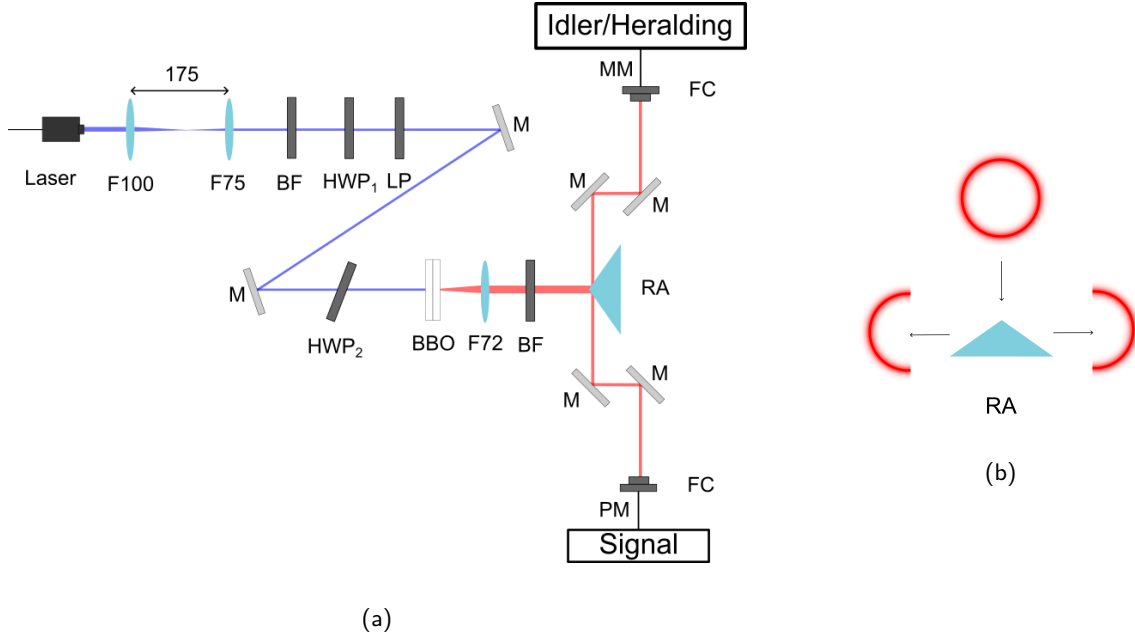


Figure 8: (a) Optical layout of the entangled photon source. (b) Single-photon beam profile after passing through the right-angle prism: the toroidal distribution is split into two semicircular lobes. By momentum conservation, this indicates that each photon of the entangled pair is directed to a separate side.

To visualize the angular emission from the BBO crystals, an axicon lens (AX255, Thorlabs) was mounted on a rotational stage and used to generate a conical reference beam. This beam mimicked the spread of SPDC emission and was aligned to propagate horizontally.

Using this as an alignment reference, the semicircles arriving at the fiber couplers were optimally coupled into the fibers with the aid of a power meter (PM100D, Thorlabs). The coupling efficiency into the multimode fibers was approximately 12 %. The pump beam incident on the axicon was 75 mW. Before the coupling lens, the reference semicircles had powers of 1.4 mW (signal arm) and 1.2 mW (heralding arm), limited by mirror reflection losses optimized for 750–1100 nm. After coupling, the power measured at the multimode fiber (M43L02, Thorlabs) outputs was 0.171 mW for the signal arm and 0.142 mW for the heralding one.

Attempts to couple the signal photons into the single-mode polarization-maintaining fiber resulted in much lower efficiencies. The measured output was just 0.6 mW, largely due to a mismatch between the SPDC beam’s spatial mode and the Gaussian mode supported by the fiber. This confirmed that either beam shaping or free-space coupling would be needed for future implementations involving single-mode transmission. In single-mode fibers, mode matching is significantly more critical than in multimode fibers, especially due to the small numerical aperture.

For the prototype, a multimode fiber (MML02, Thorlabs) was ultimately selected to collect the signal photons into the free-space channel. Although polarization is not preserved in such fibers, this did not affect basic transmission or coincidence measurements. Notably, even when using polarization-maintaining fibers, undesired polarization changes were observed [25]; misalignment between the photon polarization and the fiber axes leads to ellipticity, requiring compensation with a half-wave and quarter-wave plate pair. These observations suggest that, for future implementations of the emitter, it would be ideal

to generate the photons directly in the focal plane of the telescope to avoid polarization distortion issues altogether.

When coupling light into the multimode fibers, it is important to understand that the coupling primarily occurs from one segment of the semicircular emission pattern. An alternative route to improve coupling efficiency is to use specially engineered optical fibers that support higher-order spatial modes, such as ring modes [17]. These could better match the spatial distribution of the SPDC emission and increase the probability of detecting entangled photon pairs.

However, to ensure that both photons from the same pair are coupled, the areas of the semicircles that are primarily coupled become crucial. The photons distribute in the semicircle due to momentum conservation. To collect entangled photon pairs efficiently, it is necessary to target the regions of the emission pattern that satisfy both energy and momentum conservation. Once these well-matched regions are found by maximizing the coincidence rate between the two channels, irises can be placed to isolate and select those parts of the emission. This method not only improves the coupling of entangled pairs but also acts as a spectral filter, reducing the presence of photons with non-degenerate wavelengths [28]. This suggests that further optimization is possible.

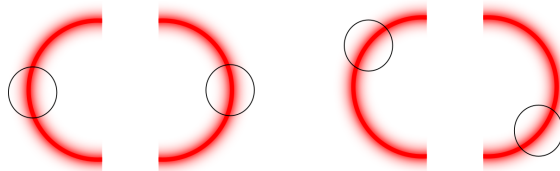


Figure 9: Optimal coupling regions in the emission pattern, based on energy conservation in the SPDC process.

3.3 Receiver

In this prototype, the role of the receiver was to detect incoming single photons and verify successful transmission through the free-space link. While a complete quantum decoder for polarization analysis would be required to implement QKD protocols, the present configuration was designed primarily for link characterization, alignment testing, and coincidence detection.

A plano-convex lens with a 35 mm focal length (LA1027-B, Thorlabs) was positioned precisely 35 mm beyond the focal plane of the telescope. This configuration ensured that the incoming light was collimated before entering the coupling optics.

The collimated beam was then directed toward the fiber input using a pair of dielectric mirrors (BB1-E03, Thorlabs), mounted to allow fine angular and lateral adjustments. These mirrors guided the beam into an 800 nm bandpass filter (FBH800-40, Thorlabs) and a fiber-coupling lens (F810FC-780, Thorlabs), which focused the light into the core of a multimode optical fiber (M43L01, Thorlabs).

Single-photon detection was performed using a four-channel detector module (SPCM-AQ4C, Excelitas Technologies). To register photon arrival times and evaluate temporal correlations, detection signals were recorded by a high-resolution time-tagger (Time Tagger Ultra, Swabian Instruments). This system enabled time-stamped detection across multiple channels, allowing for accurate coincidence measurements between photons received via the free-space link and heralding photons delivered through optical fiber.

4 Results and Discussion

4.1 Tuning the Pumping Beam

Before characterizing the entangled single-photon source, the power and spatial profile of the pump beam were optimized. For the following measurements, the BBO crystals were oriented such that the optical axis of the first BBO was nominally horizontal with respect to the optical table. No compensation was applied for the phase difference between the crystal paths, and the crystals were pumped with diagonally polarized light.

The pump power was selected based on values reported in the literature for spontaneous parametric down-conversion (SPDC) in BBO crystals [31]. The laser source had an optical output power of 315 mW. After passing through polarization control elements, phase plates, and alignment optics, the power incident on the BBO crystals was measured to be approximately 78.3 mW.

A comparison was made using a neutral density (ND) filter with an optical density (OD) of 0.2. With the filter inserted, the power incident on the crystals was reduced to 50.6 mW. Coincidence count rates were then measured: 131.18 counts per second (cps) without the filter and 71.56 cps with it, as shown in Table 1. Coincidence events were extracted by integrating over a 2 ns window centered on the peak of the correlation histogram. The values were corrected by subtracting accidental coincidences, as described in Appendix 5. Figure 10 shows the second-order cross-correlation function for the case without the OD filter. While higher pump power increases the probability of generating multiple photon pairs simultaneously [18], this effect can be considered negligible for the power levels used [14].

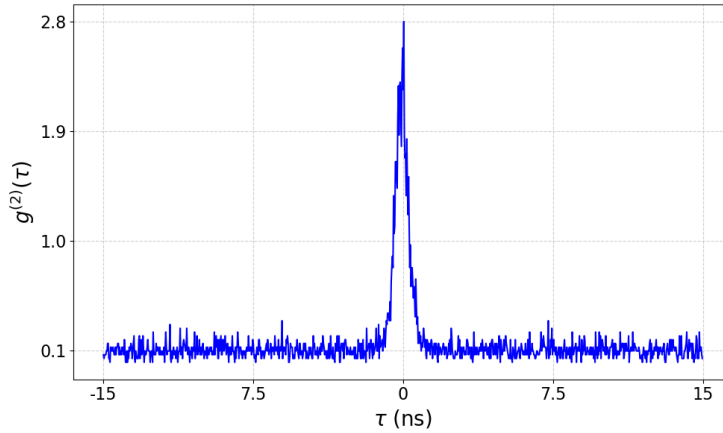


Figure 10: Second-order cross-correlation histogram (normalized). A clear coincidence peak appears at 0 ns, exceeding the noise level by 46.51σ . Bin size: 0.3 ns. Acquisition time: 17.93 s. Measurement performed without modifying the pump beam size. The incident power on the BBO crystals was 78.3 mW.

After determining the maximum operational pump power, further optimization was performed by reducing the beam diameter at the crystals, as suggested in prior work [33]. A telescope was assembled using lenses with focal lengths of 100 mm (LA1509-A, Thorlabs) and 75 mm (LA1608-A, Thorlabs), resulting in a demagnification factor of 0.75. This configuration reduced the beam waist at the BBO crystals, thereby increasing the spatial intensity of the pump.

Although this added optics introduced slight losses, reducing the power reaching the crystals to 65.5 mW, it resulted in a notable increase in detection rates: both single-

channel and coincidence counts improved. Specifically, the coincidence rate increased from 131.18 cps to 157.71 cps (see Table 1). While this increase is significant, it was not proportional to the large jump in single-channel counts, which more than doubled. This discrepancy is likely due to the system being realigned during telescope implementation. As explained in Section 3.2, this is attributed to suboptimal coupling of diametrically opposed regions of the emission ring into the collection fibers.

Measurement	Signal (cps)	Heralding (cps)
Dark counts	435.02	519.14
Noise counts (laser off)	567.14	667.38
Noise counts (laser on)	979.69	767.08
Counts (78.3 mW)	76202.13	78471.48
Coincident counts (78.3 mW)	131.18	
Counts (50.6 mW)	39904.71	40080.61
Coincident counts (50.6 mW)	71.56	
Counts (65.5 mW)*	169165.15	167089.38
Coincident counts (65.5 mW)*	157.71	

Table 1: Count rates for different measurement conditions. *Measurements marked with an asterisk were performed after beam size reduction using a demagnification telescope.

4.2 Characterization of the Entangled Photon Source

The results presented here characterize the entangled single-photon source. The rotation angle of the BBO assembly has been set to generate the desired $\frac{1}{\sqrt{2}}(|HH\rangle + |VV\rangle)$ Bell state. The relative phase between the photon-pair contributions from both BBO crystals has been corrected and a CHSH Bell test was also performed to confirm that the photon pairs are indeed entangled.

By design, the two BBO crystals are mounted orthogonally on a rotation stage. Photon pairs are generated via SPDC when the polarization of the incident pump beam aligns with the SPDC plane of one of the crystals. When horizontally polarized light is used, rotation of the BBO assembly allows identification of specific angles at which photon pairs in the $|VV\rangle$ state are predominantly produced. At these angles, one crystal’s SPDC plane is aligned with the pump polarization, enabling down-conversion, while the orthogonally oriented crystal remains inactive. Consequently, photon pairs in the $|VV\rangle$ state are emitted solely from a single crystal.

To determine these optimal emission angles, the BBO assembly was rotated in 10° increments, and coincidence counts were recorded for the polarization states $|VV\rangle$, $|VH\rangle$, $|HV\rangle$, and $|HH\rangle$. As shown in Fig. 11, the $|VV\rangle$ signal exhibits maxima at 20° , 90° , 190° , and 300° , corresponding approximately to conditions where one crystal contributes efficiently to photon-pair generation while the other remains inactive.

While a 90° periodicity is theoretically expected, deviations arise due to imperfect alignment of the BBO crystals. Specifically, the crystals are not perfectly perpendicular to the optical table, resulting in angular variations in the spatial overlap of the emitted cones during rotation. To mitigate this effect, the setup was visually inspected and realigned prior to the measurement to ensure that the coincidence counts would remain relatively stable throughout the rotation. Realignment was guided by ensuring minimal variation in both channel counts as a function of angle.

To control the relative phase between the $|VV\rangle$ and $|HH\rangle$ components generated by

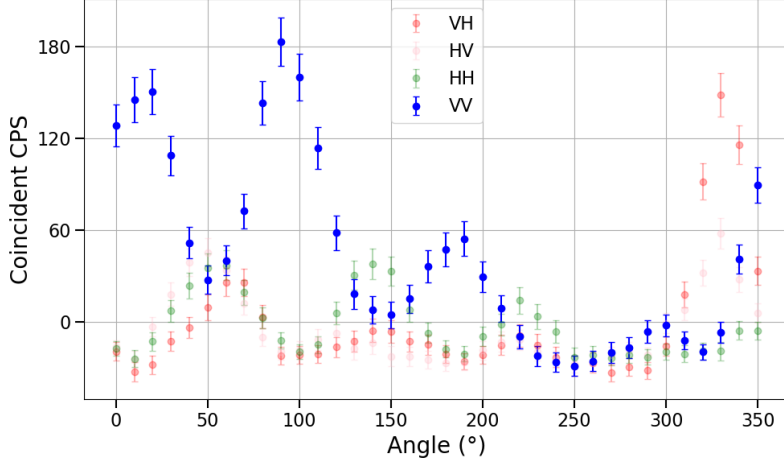


Figure 11: Coincidence cps recorded as a function of BBO rotation angle in 10° steps. Measurements were performed for multiple photon-pair polarization states. The $|VV\rangle$ state shows distinct peaks at 20° , 90° , 190° , and 300° , corresponding to optimal SPDC alignment conditions.

the two BBO crystals, a second half-wave plate ($\text{HWP}^{(2)}$) is used. This wave plate, with its fast axis aligned to the horizontal polarization, is mounted on a manual rotational platform (RP01/M, Thorlabs) allowing angular adjustment around an axis perpendicular to the optical table. By rotating $\text{HWP}^{(2)}$, the relative phase between contributions from the two crystals (Eq. 4) can be finely tuned.

When the generated state is analyzed in the $|D\rangle_S \otimes |D\rangle_I$ basis and the tilt angle φ of $\text{HWP}^{(2)}$ is varied, the coincidence rate follows the relation [31]:

$$N_{|DD\rangle}(\varphi) \propto |\langle DD|\Phi^+\rangle|^2 \propto \frac{1}{4} \cdot (1 + \cos \phi'), \quad (8)$$

where $\phi' = \phi(\varphi) + \phi_{\text{BBO}}$. Maxima and minima in the coincidence counts are observed at values of φ satisfying $\phi' = 0, \pm 2\pi$ and $\phi' = \pm\pi$, respectively. As shown in Fig. 12, maximum coincidence rates occur at $\varphi = -14^\circ, 2^\circ, 18^\circ$, while minima are found at $\varphi = -4^\circ$ and 8° .

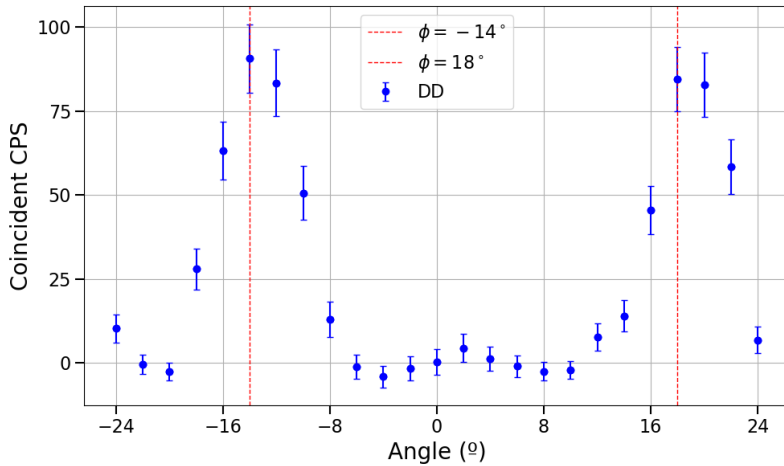


Figure 12: Coincidence CPS measured as a function of tilt angle φ of $\text{HWP}^{(2)}$ in 2° steps. Maximums are observed at -14° and 18° , consistent with constructive interference of $|VV\rangle$ and $|HH\rangle$ components.

Based on these results, the BBO crystals are fixed at a rotation angle of 90° , and

HWP₍₂₎ is set to a tilt of 18°. Under these conditions, diagonal pump polarization leads to the generation of the entangled Bell state $|\Phi^+\rangle$.

With this alignment, a Bell test was conducted to verify entanglement. Sixteen measurement settings corresponding to different combinations of polarization bases (as defined in Section 2.2.2) were used. The resulting CHSH parameter was found to be $S = 2.55 \pm 0.15$, clearly violating the classical limit of 2 and confirming the presence of quantum entanglement, although not reaching the maximal quantum value of $2\sqrt{2}$. The data measured to get to this value of S can be see in the Appendix 3 and the way to estimate the error is explained in Appendix B.

4.3 Coincident Counts Through the Link

Finally, the results of single-photon transmission through the optical link are presented. As demonstrated, a functional heralded single-photon source was successfully implemented, producing photon pairs in the entangled state $\frac{1}{\sqrt{2}}(|HH\rangle + |VV\rangle)$. One photon of each pair was directed through the optical link in order to evaluate its performance.

To verify the transmission of single photons through the link, an initial attempt was made using a 50:50 beam splitter fiber (TM50R5F1A, Thorlabs) to perform a Hanbury Brown and Twiss (HBT) experiment, with the objective of observing antibunching in the second order autocorrelation function in the received signal. However, internal reflections within the beam splitter fiber introduced artifacts, with peaks separated by 22 ns, which prevented a conclusive measurement. As a result, an alternative approach was adopted: coincidence counts were measured between the photon transmitted through a 5 m fiber and its heralding partner. While this measurement alone is not sufficient to definitively demonstrate single-photon transmission, it will be referred to as such for simplicity throughout this work. A conclusive verification would require additional measurements, such as antibunching.

To evaluate the free-space optical link, one photon of each pair was routed through a 5 m single-mode fiber (heralding), while the other was transmitted through a telescope-based free-space path (signal). The expected detection delay was calculated using the expression

$$t = \frac{n \cdot L}{c}, \quad (9)$$

where n is the refractive index, L is the propagation distance, and c is the speed of light in vacuum.

The heralding photon, propagating through 5 m of optical fiber ($n = 1.4675$), was expected to incur a delay of 24.465 ns. The signal photon, traversing 3 m of fiber and 6.9 m of air ($n = 1.0003$), including the telescope system, was expected to experience a total delay of 37.678 ns. The resulting expected detection time difference between the two channels was therefore $\Delta t = 13.213$ ns.

With the source active, the coincidence counts between heralding and signal photons were analyzed, yielding a rate of 115.34 cps, as reported in Table 2. A detection rate of approximately 100 000 cps was recorded at the output of a 2 m multimode fiber used to couple the signal photon. This value served as a baseline for estimating the transmission losses through the optical link. The second-order cross-correlation function corresponding to these counts is shown in Fig. 13, where a displaced coincidence peak is observed at approximately 15 ns. This offset is attributed to the delay introduced by coupling the heralding photons through a 5 m fiber.

To characterize background noise and optimize coupling efficiency, dark counts and signal levels were recorded under several conditions, as summarized in Table 2. As de-

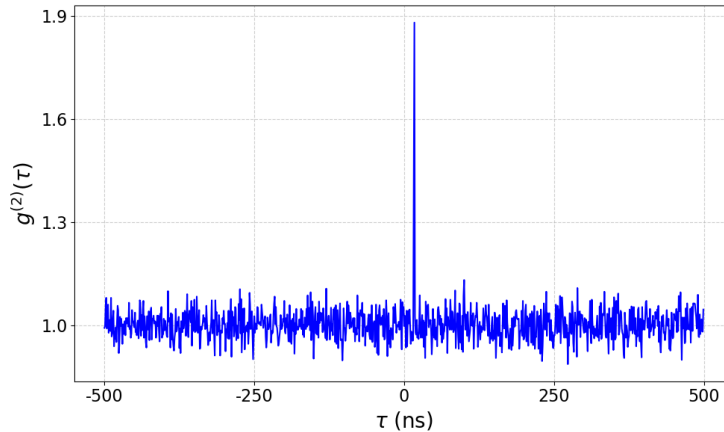


Figure 13: Second-order cross-correlation histogram (normalized). A clear coincidence peak appears at 17 ns, exceeding the noise level by 21.83σ . Bin size: 1 ns. Acquisition time: 20.93 s.

scribed in Section 3.1, light was coupled from fiber to free space using a fiber collimator (F810FC-780) and a demagnification telescope.

Measurement	Signal (cps)	Heralding (cps)
Dark counts	435.02	519.14
Noise counts (laser off)	2154.18	597.91
Noise counts (laser on)	2312.40	782.60
Counts (source on)	124726.60	213974.25
Coincident counts (source)	115.34	
Counts (Axicons setup)	2291.46	215987.33
Counts (Displaced beam)	2214.22	211776.88
Counts (Displaced beam*)	5092.15	219111.25
Coincident counts (Displaced beam*)	0.74	

Table 2: Count rates under various measurement conditions. *These measurements were performed removing the collimation lenses.

Several emitter configurations for the signal photons were tested, including axicon-based and beam-displacement configurations.

In the first configuration, based on the axicon setup described in Section 3.1, alignment was performed using a 635 nm lamp with a power of approximately 2 mW (VLP50, NetPeppers). A power of $36\ \mu\text{W}$ was measured at the receiver input, mainly limited by losses from IR-optimized coupling mirrors. Of this, $4\ \mu\text{W}$ was successfully coupled into the multimode fiber, resulting in a coupling efficiency of 11.1%. The beam observed at the telescope focal plane is shown in Fig. 14a, where distortions can be seen despite nominal alignment.

However, no significant signal above the noise level was observed for the quantum signal. This was attributed to poor mode-matching between the ring-shaped beam generated by the axicons and the fiber mode. A potential solution may involve adding a second axicon stage to reconvert the beam into a Gaussian profile, which would be more compatible with multimode fiber coupling.

In the second configuration, the axicons were removed and the beam was laterally displaced to avoid central obstruction from the telescope. Classical coupling measurements yielded a received power of $236\ \mu\text{W}$, with $5\ \mu\text{W}$ coupled into the fiber, corresponding to

a coupling efficiency of 2.12%. The beam profile at the receiver is shown in Fig. 14b. However, no significant signal above the noise level was observed for the quantum signal, attributed to losses in the optical elements.

In the third configuration, both the achromatic lens (9-794, Edmund Optics) and the 35 mm focal length (LA1027-B, ThorLabs) telescope lenses were removed to eliminate optical losses. Although the beam divergence increased and the beam was not perfectly collimated, the effect was considered negligible due to the short link distance. Classical alignment using the red laser source yielded 260 μW at the receiver, with 50 μW coupled into the fiber, corresponding to a coupling efficiency of 19.2%. Under this configuration, a signal detection rate of approximately 5000 cps (see Table 2) was achieved at the receiver, almost 3000 cps above the noise level. The corresponding second-order cross-correlation function is shown in Fig. 15, where a distinct coincidence peak at -13 ns confirms successful single-photon transmission through the free-space link. The acquisition time was 15 minutes, yielding a coincident count rate of 44.4 counts per minute (cpm). The peak exceeds the noise level by 8.70σ .



Figure 14: Beam images captured at the receiver using a CMOS sensor. (a) Beam at the telescope focal plane using the axicon configuration. (b) Beam profile using the displaced beam configuration.

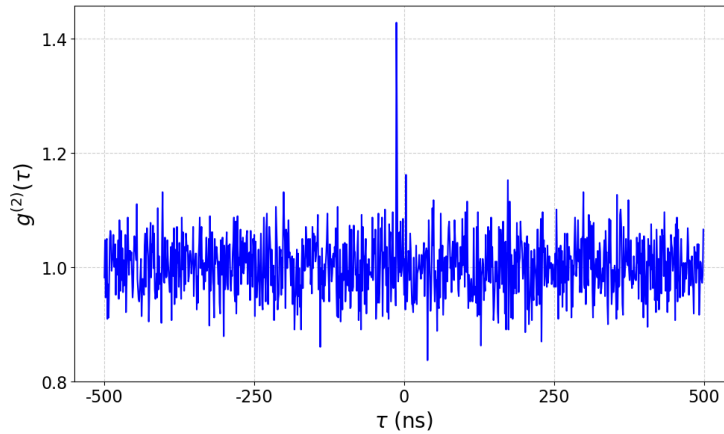


Figure 15: Second-order cross-correlation histogram (normalized). A clear coincidence peak appears at -13 ns, exceeding the noise level by 8.70σ . Bin size: 1 ns. Acquisition time: 15 min.

Despite the coincident count rate being low, it is worth noting that a count rate of approximately 5000 cps, around 3000 cps above the noise level, was detected at the receiver. These are most likely single photons. The coincident counts could be improved by ensuring proper coupling of the entangled-photon source (Section 3.2).

4.4 Discussion of Key Rates

A measured coincidence rate of approximately 44.4 cpm was obtained. Based on this, the potential secret key rate for a BB84 quantum key distribution (QKD) implementation can be estimated. Since BB84 requires random and independent basis choices on both sides, only about 50% of the detected photon pairs are expected to contribute to the sifted key. As a result, the sifted coincidence rate is reduced to 22.2 counts per minute, corresponding to approximately 0.37 bits per second (assuming one bit per coincidence count).

Assuming a low quantum bit error rate (QBER) of $e = 2\%$, and applying the asymptotic key rate formula [32]:

$$R = S[1 - 2h(e)], \quad (10)$$

where $h(e)$ is the binary entropy function, the following estimate is obtained:

$$R \approx 0.37 \cdot (1 - 2 \cdot h(0.02)) \approx 0.37 \cdot 0.718 = 0.27 \text{ bits/sec.} \quad (11)$$

While long-distance communication was not the primary objective of this experiment, future implementations could consider establishing a free-space optical link to more distant locations, such as the Fabra Observatory, located approximately 4 km away. Over such distances, urban free-space channels typically introduce atmospheric losses in the range of 15-25 dB due to absorption, turbulence, and misalignment. Assuming a conservative total loss of 20 dB, a reduction in the coincidence rate by a factor of 100 would be expected, yielding:

$$R_{\text{Fabra}} \approx 0.27 \cdot 10^{-2} \text{ bits/sec.} \quad (12)$$

To achieve a practically useful key rate at such distances (e.g., 100-500 bits/sec), an increase in the raw coincidence rate by several orders of magnitude would be required, reaching values between 20,000 and 140,000 cps before transmission. This estimate does not yet account for additional reductions due to error correction [16] or privacy amplification [42].

To significantly improve photon transmission and simplify alignment, it is suggested that the single-photon source be placed directly behind the emitter telescope in future designs. This configuration would eliminate the need for coupling into single-mode fibers and would avoid polarization drifts and temporal dispersion effects introduced by long optical fibers. Ideally, the receiver should also be positioned immediately after the second telescope, using only short multimode fibers for detection.

An additional improvement could involve replacing the current SPDC source that emits photons in a Gaussian spatial mode. This would enhance mode matching with the telescope optics, especially in the axicon-based configuration, and could significantly increase the coupling efficiency. Nonetheless, the current source, despite producing a non-Gaussian beam, can still be adapted for free-space transmission by spatially filtering the emission with irises to approximate a Gaussian profile.

5 Conclusions

The main objective of this Master's thesis was to demonstrate single-photon transmission over a free-space optical link. This objective has been achieved successfully.

Single photons have been transmitted across a 1.88 m free-space link using Ritchey-Chrétien telescopes. The detection system confirmed the arrival of heralded single photons

above background noise. A coincidence peak of 44.4 cpm in the cross-correlation function has been measured, verifying successful transmission and detection.

The free-space link has been implemented using Ritchey–Chrétien reflective telescopes. Two strategies have been tested to overcome the telescopes’ central obstruction: generating a toroidal Bessel-like beam using axicons, and laterally displacing the beam. Successful transmission has been achieved using the lateral displacement method.

An entangled photon source has been built using a two-crystal SPDC configuration with BBO crystals. The rotation of the crystal mount has been calibrated, and the phase between the $|HH\rangle$ and $|VV\rangle$ components has been tuned using a half-wave plate. The presence of entanglement has been confirmed by a CHSH Bell test, which gave a Bell parameter of $S = 2.55 \pm 0.15$, exceeding the classical limit.

Future developments will focus on optimizing the optical link by positioning the single-photon source directly at the focal plane of the transmitting telescope. This will ideally increase the single-photon detection rate and their polarization will be preserved.

The axicon-based method can be further studied using a source with a Gaussian spatial mode.

The effects of humidity on the transmission channel can be investigated. Changes in laboratory temperature, controlled through the air conditioning system, can modify the relative humidity and may influence beam quality and photon detection. Active wavefront correction can be implemented to improve the stability of the optical link under environmental changes. This work is planned in collaboration with institutions such as Universitat Ramon Llull.

Finally, experiments can be extended to longer free-space distances to evaluate the scalability of the setup.

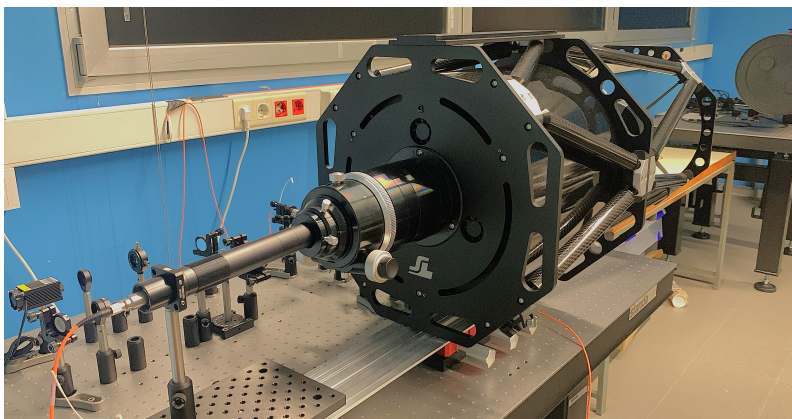


Figure 16: Experimental set-up for the laboratory-based FSO quantum link developed during this Master’s thesis.

Bibliography

- [1] *Adaptive optics benefit for quantum key distribution uplink from ground to a satellite*. URL: <https://www.degruyterbrill.com/document/doi/10.1515/aot-2020-0017/html>.
- [2] Igor Aharonovich and Elke Neu. “Diamond Nanophotonics”. In: *Advanced Optical Materials* 2.10 (2014), pp. 911–928. ISSN: 2195-1071. DOI: [10.1002/adom.201400189](https://doi.org/10.1002/adom.201400189). URL: <https://onlinelibrary.wiley.com/doi/abs/10.1002/adom.201400189>.
- [3] O Alibart et al. “Photon pair generation using four-wave mixing in a microstructured fibre: theory versus experiment”. In: *New Journal of Physics* 8.5 (May 2006), p. 67. ISSN: 1367-2630. DOI: [10.1088/1367-2630/8/5/067](https://doi.org/10.1088/1367-2630/8/5/067). URL: <https://dx.doi.org/10.1088/1367-2630/8/5/067>.
- [4] Charles H. Bennett et al. “Experimental quantum cryptography”. In: *Journal of Cryptology* 5.1 (Jan. 1, 1992), pp. 3–28. ISSN: 1432-1378. DOI: [10.1007/BF00191318](https://doi.org/10.1007/BF00191318). URL: <https://doi.org/10.1007/BF00191318>.
- [5] J-P Bourgoin et al. “A comprehensive design and performance analysis of low Earth orbit satellite quantum communication”. In: *New Journal of Physics* 15.2 (Feb. 2013). Publisher: IOP Publishing, p. 023006. ISSN: 1367-2630. DOI: [10.1088/1367-2630/15/2/023006](https://doi.org/10.1088/1367-2630/15/2/023006). URL: <https://dx.doi.org/10.1088/1367-2630/15/2/023006>.
- [6] Gabriela Calistro-Rivera et al. *Building Europe’s first space-based Quantum Key Distribution system – The German Aerospace Center’s role in the EAGLE-1 mission*. Dec. 4, 2024. DOI: [10.48550/arXiv.2412.03222](https://doi.org/10.48550/arXiv.2412.03222). arXiv: [2412.03222\[quant-ph\]](https://arxiv.org/abs/2412.03222). URL: <http://arxiv.org/abs/2412.03222>.
- [7] S. A. Castelletto and R. E. Scholten. “Heralded single photon sources: a route towards quantum communication technology and photon standards”. In: *The European Physical Journal - Applied Physics* 41.3 (Mar. 2008), pp. 181–194. ISSN: 1286-0042, 1286-0050. DOI: [10.1051/epjap:2008029](https://doi.org/10.1051/epjap:2008029). URL: <https://www.cambridge.org/core/journals/the-european-physical-journal-applied-physics/article/abs/heralded-single-photon-sources-a-route-towards-quantum-communication-technology-and-photon-standards/OFA33D645699C206C639A136F494F1BF>.
- [8] John F. Clauser et al. “Proposed Experiment to Test Local Hidden-Variable Theories”. In: *Physical Review Letters* 23.15 (Oct. 13, 1969). Publisher: American Physical Society, pp. 880–884. DOI: [10.1103/PhysRevLett.23.880](https://doi.org/10.1103/PhysRevLett.23.880). URL: <https://link.aps.org/doi/10.1103/PhysRevLett.23.880>.
- [9] Dietrich Dehlinger and M. W. Mitchell. “Entangled photon apparatus for the undergraduate laboratory”. In: *American Journal of Physics* 70.9 (Sept. 1, 2002), pp. 898–902. ISSN: 0002-9505. DOI: [10.1119/1.1498859](https://doi.org/10.1119/1.1498859). URL: <https://doi.org/10.1119/1.1498859>.
- [10] *Full article: Spontaneous parametric down-conversion*. URL: https://www.tandfonline.com/doi/full/10.1080/00107514.2018.1488463?casa_token=I3Lz-JnAYggAAAAA%3ALWkBKOn_116Y7P4RqCqoxb5eQzxi1YHx7-UWrcqJFgpAS425vkPzkdUfT7kj5ARiuVpWUtjB1a8.
- [11] Helmuth Horvath. “Light absorption in the atmosphere”. In: *Light Scattering Reviews 10: Light Scattering and Radiative Transfer*. Ed. by Alexander A. Kokhanovsky. Berlin, Heidelberg: Springer, 2016, pp. 235–289. ISBN: 978-3-662-46762-6. DOI: [10.1007/978-3-662-46762-6_6](https://doi.org/10.1007/978-3-662-46762-6_6). URL: https://doi.org/10.1007/978-3-662-46762-6_6.
- [12] H. J. Kimble, M. Dagenais, and L. Mandel. “Photon Antibunching in Resonance Fluorescence”. In: *Physical Review Letters* 39.11 (Sept. 12, 1977). Publisher: American Physical Society, pp. 691–695. DOI: [10.1103/PhysRevLett.39.691](https://doi.org/10.1103/PhysRevLett.39.691). URL: <https://link.aps.org/doi/10.1103/PhysRevLett.39.691>.
- [13] Axel Kuhn, Markus Hennrich, and Gerhard Rempe. “Deterministic Single-Photon Source for Distributed Quantum Networking”. In: *Physical Review Letters* 89.6 (July 19, 2002). Publisher: American Physical Society, p. 067901. DOI: [10.1103/PhysRevLett.89.067901](https://doi.org/10.1103/PhysRevLett.89.067901). URL: <https://link.aps.org/doi/10.1103/PhysRevLett.89.067901>.

- [14] Paul G. Kwiat et al. “Ultrabright source of polarization-entangled photons”. In: *Physical Review A* 60.2 (Aug. 1, 1999). Publisher: American Physical Society, R773–R776. DOI: [10.1103/PhysRevA.60.R773](https://doi.org/10.1103/PhysRevA.60.R773). URL: <https://link.aps.org/doi/10.1103/PhysRevA.60.R773>.
- [15] Sang Min Lee et al. “Polarization-entangled photon-pair source obtained via type-II non-collinear SPDC process with PPKTP crystal”. In: *Optics Express* 24.3 (Feb. 8, 2016). Publisher: Optica Publishing Group, pp. 2941–2953. ISSN: 1094-4087. DOI: [10.1364/OE.24.002941](https://doi.org/10.1364/OE.24.002941). URL: <https://opg.optica.org/oe/abstract.cfm?uri=oe-24-3-2941>.
- [16] Wei-Yue Liu et al. “Experimental free-space quantum key distribution with efficient error correction”. In: *Optics Express* 25.10 (May 15, 2017). Publisher: Optica Publishing Group, pp. 10716–10723. ISSN: 1094-4087. DOI: [10.1364/OE.25.010716](https://doi.org/10.1364/OE.25.010716). URL: <https://opg.optica.org/oe/abstract.cfm?uri=oe-25-10-10716>.
- [17] Yuanpeng Liu et al. “Parabolic-Index Ring-Core Fiber Supporting High-Purity Orbital Angular Momentum Modes”. In: *Sensors* 23.7 (Jan. 2023). Number: 7 Publisher: Multidisciplinary Digital Publishing Institute, p. 3641. ISSN: 1424-8220. DOI: [10.3390/s23073641](https://doi.org/10.3390/s23073641). URL: <https://www.mdpi.com/1424-8220/23/7/3641>.
- [18] Xiao-song Ma et al. “Experimental generation of single photons via active multiplexing”. In: *Physical Review A* 83.4 (Apr. 13, 2011). Publisher: American Physical Society, p. 043814. DOI: [10.1103/PhysRevA.83.043814](https://doi.org/10.1103/PhysRevA.83.043814). URL: <https://link.aps.org/doi/10.1103/PhysRevA.83.043814>.
- [19] Ivan Marcikic, Antía Lamas-Linares, and Christian Kurtsiefer. “Free-space quantum key distribution with entangled photons”. In: *Applied Physics Letters* 89.10 (Sept. 8, 2006), p. 101122. ISSN: 0003-6951. DOI: [10.1063/1.2348775](https://doi.org/10.1063/1.2348775). URL: <https://doi.org/10.1063/1.2348775>.
- [20] Lluís Masanes, Stefano Pironio, and Antonio Acín. “Secure device-independent quantum key distribution with causally independent measurement devices”. In: *Nature Communications* 2.1 (Mar. 15, 2011). Publisher: Nature Publishing Group, p. 238. ISSN: 2041-1723. DOI: [10.1038/ncomms1244](https://doi.org/10.1038/ncomms1244). URL: <https://www.nature.com/articles/ncomms1244>.
- [21] G. Messin et al. “Bunching and antibunching in the fluorescence of semiconductor nanocrystals”. In: *Optics Letters* 26.23 (Dec. 1, 2001). Publisher: Optica Publishing Group, pp. 1891–1893. ISSN: 1539-4794. DOI: [10.1364/OL.26.001891](https://doi.org/10.1364/OL.26.001891). URL: <https://opg.optica.org/ol/abstract.cfm?uri=ol-26-23-1891>.
- [22] *Micius quantum experiments in space* / *Rev. Mod. Phys.* URL: <https://journals.aps.org/rmp/abstract/10.1103/RevModPhys.94.035001>.
- [23] Alexander Miller. “Micius, the world’s first quantum communication satellite, was hackable”. In: *2025 International Conference on Quantum Communications, Networking, and Computing (QCNC)*. 2025 International Conference on Quantum Communications, Networking, and Computing (QCNC). Mar. 2025, pp. 411–415. DOI: [10.1109/QCNC64685.2025.00070](https://doi.org/10.1109/QCNC64685.2025.00070). URL: <https://ieeexplore.ieee.org/abstract/document/11000231>.
- [24] Kimia Mohammadi. “Design and Characterization of a Transceiver Telescope for Quantum Communications with Satellites”. In: (Sept. 30, 2021). Publisher: University of Waterloo. URL: <http://hdl.handle.net/10012/17599>.
- [25] J. Noda, K. Okamoto, and Y. Sasaki. “Polarization-maintaining fibers and their applications”. In: *Journal of Lightwave Technology* 4.8 (Aug. 1986), pp. 1071–1089. ISSN: 1558-2213. DOI: [10.1109/JLT.1986.1074847](https://doi.org/10.1109/JLT.1986.1074847). URL: <https://ieeexplore.ieee.org/abstract/document/1074847>.
- [26] K. A. Patel et al. “Coexistence of High-Bit-Rate Quantum Key Distribution and Data on Optical Fiber”. In: *Physical Review X* 2.4 (Nov. 20, 2012). Publisher: American Physical Society, p. 041010. DOI: [10.1103/PhysRevX.2.041010](https://doi.org/10.1103/PhysRevX.2.041010). URL: <https://link.aps.org/doi/10.1103/PhysRevX.2.041010>.

- [27] Asher Peres. “All the Bell Inequalities”. In: *Foundations of Physics* 29.4 (Apr. 1, 1999), pp. 589–614. ISSN: 1572-9516. DOI: [10.1023/A:1018816310000](https://doi.org/10.1023/A:1018816310000). URL: <https://doi.org/10.1023/A:1018816310000>.
- [28] Radhika Rangarajan, Michael Goggin, and Paul Kwiat. “Optimizing type-I polarization-entangled photons”. In: *Optics Express* 17.21 (Oct. 12, 2009). Publisher: Optica Publishing Group, pp. 18920–18933. ISSN: 1094-4087. DOI: [10.1364/OE.17.018920](https://doi.org/10.1364/OE.17.018920). URL: <https://opg.optica.org/oe/abstract.cfm?uri=oe-17-21-18920>.
- [29] N. Martínez Rey, L. F. Rodríguez Ramos, and Z. Sodnik. “Uplink wavefront corrector system: from paper to reality”. In: *Optics Express* 28.5 (Mar. 2, 2020). Publisher: Optica Publishing Group, pp. 5886–5897. ISSN: 1094-4087. DOI: [10.1364/OE.28.005886](https://doi.org/10.1364/OE.28.005886). URL: <https://opg.optica.org/oe/abstract.cfm?uri=oe-28-5-5886>.
- [30] A.A.M. Saleh. “9.4 - An investigation of laser wave depolarization due to atmospheric transmission”. In: *IEEE Journal of Quantum Electronics* 3.11 (Nov. 1967), pp. 540–543. ISSN: 1558-1713. DOI: [10.1109/JQE.1967.1074404](https://doi.org/10.1109/JQE.1967.1074404). URL: <https://ieeexplore.ieee.org/document/1074404>.
- [31] Raul Lahoz Sanz et al. “Undergraduate setup for measuring the Bell inequalities and performing quantum state tomography”. In: *EPJ Quantum Technology* 11.1 (Dec. 1, 2024). Number: 1 Publisher: Springer Berlin Heidelberg, p. 86. ISSN: 2662-4400, 2196-0763. DOI: [10.1140/epjqt/s40507-024-00298-y](https://doi.org/10.1140/epjqt/s40507-024-00298-y). URL: https://epjqt.epj.org/articles/epjqt/abs/2024/01/40507_2024_Article_298/40507_2024_Article_298.html.
- [32] Valerio Scarani et al. “The security of practical quantum key distribution”. In: *Reviews of Modern Physics* 81.3 (Sept. 29, 2009). Publisher: American Physical Society, pp. 1301–1350. DOI: [10.1103/RevModPhys.81.1301](https://doi.org/10.1103/RevModPhys.81.1301). URL: <https://link.aps.org/doi/10.1103/RevModPhys.81.1301>.
- [33] Nicolas Schwaller et al. “Optimizing the coupling efficiency of spontaneous parametric down-conversion photon pairs into single-mode fibers”. In: *Physical Review A* 106.4 (Oct. 28, 2022). Publisher: American Physical Society, p. 043719. DOI: [10.1103/PhysRevA.106.043719](https://doi.org/10.1103/PhysRevA.106.043719). URL: <https://link.aps.org/doi/10.1103/PhysRevA.106.043719>.
- [34] Pascale Senellart, Glenn Solomon, and Andrew White. “High-performance semiconductor quantum-dot single-photon sources”. In: *Nature Nanotechnology* 12.11 (Nov. 2017). Publisher: Nature Publishing Group, pp. 1026–1039. ISSN: 1748-3395. DOI: [10.1038/nnano.2017.218](https://doi.org/10.1038/nnano.2017.218). URL: <https://www.nature.com/articles/nnano.2017.218>.
- [35] Kapil Kumar Soni and Akhtar Rasool. “Cryptographic Attack Possibilities over RSA Algorithm through Classical and Quantum Computation”. In: *2018 International Conference on Smart Systems and Inventive Technology (ICSSIT)*. 2018 International Conference on Smart Systems and Inventive Technology (ICSSIT). Dec. 2018, pp. 11–15. DOI: [10.1109/ICSSIT.2018.8748675](https://doi.org/10.1109/ICSSIT.2018.8748675). URL: <https://ieeexplore.ieee.org/abstract/document/8748675>.
- [36] *Spontaneous Parametric Down-Conversion Sources for Multiphoton Experiments - Zhang - 2021 - Advanced Quantum Technologies - Wiley Online Library*. URL: <https://onlinelibrary.wiley.com/doi/abs/10.1002/qute.202000132>.
- [37] Fabian Steinlechner. “Sources of photonic entanglement for applications in space”. Accepted: 2016-11-09T13:20:28Z Publication Title: TDX (Tesis Doctorals en Xarxa). Doctoral thesis. Universitat Politècnica de Catalunya, Dec. 14, 2015. DOI: [10.5821/dissertation-2117-96057](https://doi.org/10.5821/dissertation-2117-96057). URL: <https://upcommons.upc.edu/handle/2117/96057>.
- [38] Hiroki Takesue et al. “Quantum key distribution over a 40-dB channel loss using superconducting single-photon detectors”. In: *Nature Photonics* 1.6 (June 2007). Publisher: Nature Publishing Group, pp. 343–348. ISSN: 1749-4893. DOI: [10.1038/nphoton.2007.75](https://doi.org/10.1038/nphoton.2007.75). URL: <https://www.nature.com/articles/nphoton.2007.75>.
- [39] Anastasija Trizna and Andris Ozols. “An Overview of Quantum Key Distribution Protocols”. In: *Information Technology and Management Science* 21 (Dec. 14, 2018), pp. 37–44. ISSN: 2255-9094, 2255-9086. DOI: [10.7250/itms-2018-0005](https://doi.org/10.7250/itms-2018-0005). URL: <https://itms-journals.rtu.lv/article/view/itms-2018-0005>.

- [40] R. Ursin et al. “Free-Space distribution of entanglement and single photons over 144 km”. In: *Nature Physics* 3.7 (July 2007), pp. 481–486. ISSN: 1745-2473, 1745-2481. DOI: [10.1038/nphys629](https://doi.org/10.1038/nphys629). arXiv: [quant - ph / 0607182](https://arxiv.org/abs/quant-ph/0607182). URL: <http://arxiv.org/abs/quant-ph/0607182>.
- [41] D. Vasylyev, A. A. Semenov, and W. Vogel. “Atmospheric Quantum Channels with Weak and Strong Turbulence”. In: *Physical Review Letters* 117.9 (Aug. 23, 2016). Publisher: American Physical Society, p. 090501. DOI: [10.1103/PhysRevLett.117.090501](https://doi.org/10.1103/PhysRevLett.117.090501). URL: <https://link.aps.org/doi/10.1103/PhysRevLett.117.090501>.
- [42] Yodai Watanabe. “Privacy amplification for quantum key distribution”. In: *Journal of Physics A: Mathematical and Theoretical* 40.3 (Dec. 2006), F99. ISSN: 1751-8121. DOI: [10.1088/1751-8113/40/3/F03](https://doi.org/10.1088/1751-8113/40/3/F03). URL: <https://dx.doi.org/10.1088/1751-8113/40/3/F03>.
- [43] Yichen Zhang et al. “Continuous-variable QKD over 50 km commercial fiber”. In: *Quantum Science and Technology* 4.3 (May 2019). Publisher: IOP Publishing, p. 035006. ISSN: 2058-9565. DOI: [10.1088/2058-9565/ab19d1](https://doi.org/10.1088/2058-9565/ab19d1). URL: <https://dx.doi.org/10.1088/2058-9565/ab19d1>.

A Coincident Counts

The calculation of the coincident cps was performed following the procedure described here. Starting from the unnormalized second-order autocorrelation function, represented as a histogram of time differences between detection events, the number of counts around the peak of the distribution was integrated.

The bin with the maximum number of counts, corresponding to the most probable coincidence time, was identified. An integration window of 2 ns was then centered around this peak, and all counts within this window were summed. The result was normalized by the total acquisition time, yielding the raw coincident counts in cps.

To account for accidental coincidences, the count rates in each detection channel, N_1 and N_2 (in cps), were used. The accidental coincidence rate was estimated as

$$N_{\text{acc}} = \frac{N_1 \cdot N_2 \cdot \tau}{T} \quad (13)$$

where τ is the width of the coincidence window in seconds and T is the total acquisition time.

The corrected coincident count rate was obtained by subtracting the estimated accidental coincidences from the raw coincidence rate:

$$N_c = N - N_{\text{acc}} \quad (14)$$

All quantities are reported in counts per second.

B Probabilities and Uncertainties

The calculation of probabilities and uncertainties was performed following the procedure described in [31]. Assuming that the detection counts are governed by Poisson statistics, the uncertainty in the number of detected events during a fixed time interval corresponds to the square root of the event count. Thus,

$$\sigma_{N_a} = \sqrt{N_a}, \quad \sigma_{N_b} = \sqrt{N_b}, \quad \sigma_{N_c} = \sqrt{N_c} \quad (15)$$

Applying standard error propagation to the expression for the accidental coincidences, the uncertainty in N_{acc} is given by:

$$\sigma_{N_{\text{acc}}} = \frac{\tau}{T} \cdot \sqrt{N_b^2 \cdot \sigma_{N_a}^2 + N_a^2 \cdot \sigma_{N_b}^2} = \frac{\tau}{T} \cdot \sqrt{N_b^2 \cdot N_a + N_a^2 \cdot N_b} \quad (16)$$

Here, τ is the coincidence window and T is the total acquisition time, both considered as known constants with negligible uncertainty. To simplify notation, the number of true coincidence events is defined as

$$N_{VV} = N(|V_\alpha V_\beta\rangle) = N_c(|V_\alpha V_\beta\rangle) - N_{\text{acc}}(|V_\alpha V_\beta\rangle) \quad (17)$$

with associated uncertainty:

$$\sigma_{N_{VV}} = \sqrt{\sigma_{N_c}^2(|V_\alpha V_\beta\rangle) + \sigma_{N_{\text{acc}}}^2(|V_\alpha V_\beta\rangle)} \quad (18)$$

The probability for detecting a given polarization combination is calculated as

$$P_{|V_\alpha V_\beta\rangle} = \frac{N_{|V_\alpha V_\beta\rangle}}{N_{|V_\alpha V_\beta\rangle} + N_{|V_{\alpha+90^\circ} V_\beta\rangle} + N_{|V_\alpha V_{\beta+90^\circ}\rangle} + N_{|V_{\alpha+90^\circ} V_{\beta+90^\circ}\rangle}} \quad (19)$$

which simplifies to

$$P_{|V_\alpha V_\beta\rangle} = \frac{N_{VV}}{N_{VV} + N_{VH} + N_{HV} + N_{HH}} \quad (20)$$

Since $|V_{\alpha+90^\circ}\rangle = |H_\alpha\rangle$, the uncertainty in the probability is given by:

$$\sigma_{P_{|V_\alpha V_\beta\rangle}} = \frac{N_{VV}^2 \cdot (\sigma_{N_{VH}}^2 + \sigma_{N_{HV}}^2 + \sigma_{N_{HH}}^2) + (N_{HV} + N_{VH} + N_{HH})^2 \cdot \sigma_{N_{VV}}^2}{(N_{VV} + N_{HH} + N_{VH} + N_{HV})^2} \quad (21)$$

The total uncertainty in the correlation function $E_{\alpha,\beta}$ is then

$$\sigma_{E_{\alpha,\beta}} = \sqrt{\sigma_{P_{|V_\alpha V_\beta\rangle}}^2 + \sigma_{P_{|V_\alpha H_\beta\rangle}}^2 + \sigma_{P_{|H_\alpha V_\beta\rangle}}^2 + \sigma_{P_{|H_\alpha H_\beta\rangle}}^2} \quad (22)$$

The uncertainty in the Bell parameter S is given by

$$\sigma_S = \sqrt{\sigma_{E_{\alpha,\beta}}^2 + \sigma_{E_{\alpha,\beta'}}^2 + \sigma_{E_{\alpha',\beta}}^2 + \sigma_{E_{\alpha',\beta'}}^2} \quad (23)$$

C Bell Test Experimental Data

α ($^\circ$)	β ($^\circ$)	N_a (cps)	N_b (cps)	N_{acc} (cps)	N_c (cps)
0	22.5	81077.63	55870.13	9.01	104.11
90	22.5	75649.86	55387.71	8.34	16.56
0	112.5	84148.10	63753.10	10.68	5.75
90	112.5	76991.56	64282.77	9.85	17.66
45	22.5	78704.2	55054.2	8.62	101.74
135	22.5	79001.57	55512.57	8.73	27.28
45	112.5	80639.38	64142.75	10.29	4.36
135	112.5	79106.18	63594.45	10.01	19.01
0	-22.5	84460.50	41144.08	6.91	67.40
90	-22.5	79244.30	41019.3	6.46	-0.46
0	67.5	83888.20	62831.90	10.49	4.67
90	67.5	78908.57	62965.14	9.89	50.48
45	-22.5	83129.60	41333.60	6.84	31.66
135	-22.5	81146.20	41185.40	6.65	39.60
45	67.5	82083.71	62762.86	10.25	44.19
135	67.5	80891.33	62810.56	10.11	9.25

Table 3: Data obtained for the calculation of the Bell inequality using photon pairs in the $|\Phi^+\rangle$ state. N_a refers to the signal channel, N_b to the heralding channel, N_{acc} to the accidental coincidence counts, and N_c is the total number of true coincidences after correcting for N_{acc} .

D List of Material

Product	Reference	Price (eur.)	Quantity
Emitter Telescope	GSRC12Truss, TS-Optics	4190.00	1
Receiver Telescope	GSRC12C, TS-Optics	4398.00	1
Laser 405nm, 500mW	AliExpress	26.39	1
USB Laser 405nm, 1mW	PL205, ThorLabs	224.22	1
BBO crystals	EKSMA Optics	1540.00	1
BBO crystals mount	KS1RS, ThorLabs	250.90	1
Axicons	AX255-A, ThorLabs	577.71	2
Right-Angle Prism	MRAK25-P01, ThorLabs	132.82	1
Fiber-coupling lenses	F810FC-780, ThorLabs	267.73	4
75mm PC Lens	LA1608-A, ThorLabs	35.97	1
100mm PC Lens	LA1509-A, ThorLabs	35.12	1
125mm PC Lens	LA1986-B, ThorLabs	35.12	1
35mm PC Lens	LA1027-B, ThorLabs	37.38	2
Achromatic Lens	49-794, Edmund Optics	125.66	2
Dichroic Filters	34-737, Edmund Optics	502.64	2
Bandpass Filter 405 nm	FBH405-10, ThorLabs	149.69	1
Bandpass Filter 800 nm	FBH800-40, ThorLabs	149.69	4
'Infrared' Polarizer	LPNIRE100-B, ThorLabs	116.46	2
'Visible' Polarizer	LPVISE100-A, ThorLabs	103.08	1
Half-wave Plate 405 nm	WPH05M-405, ThorLabs	461.09	2
Mirrors	BB1-E02, ThorLabs	73.83	2
Mirrors	BB1-E03, ThorLabs	73.83	6
Kinematic mount	KM100, ThorLabs	38.04	8
Goniometer	RP01/M, ThorLabs	101.24	1
Rotation Mount	RSP1X225/M, ThorLabs	141.46	4
Platform Mount	BSH1/M, ThorLabs	49.67	1
Dichroic Filter Mount	CM1-DCH/M, ThorLabs	187.17	1
1 m MM Fiber	M43L01, ThorLabs	81.73	1
2 m MM Fiber	M43L02, ThorLabs	85.04	2
5 m MM Fiber	M43L05, ThorLabs	94.38	1
PM Fiber	P3-630PM-FC-2, ThorLabs	244.85	1
BS Fiber	TM50R5F1A, ThorLabs	334.75	1
4-channel detector	SPCM-AQ4C, Excelitas Technologies	13456.21	1
Time-tagger Module	TTUltra, Swabian Instruments	11990.00	1

Table 4: Detailed equipment used in the setups. Mechanical elements such as optical tables, breadboards, posts, post-holders, clamps, tubes and customized pieces are not included.